Supplementary information

Decoding Non-Faradaic Signal Transduction in Organic Electrochemical Transistor Based Biosensors

Luca Salvigni[1], Prem Depan Nayak[1], Anil Koklu[1], Raphaela Silva[1], Adel Hama[1], Raik Grünberg[2], Stefan T. Arold[2], Sahika Inal[1*]

[1]Organic Bioelectronics Laboratory, Division of Biomedical Sciences, KAUST, Thuwal 23955-6900, Saudi Arabia.

[2]KAUST Center of Excellence for Smart Health, Division of Biomedical Sciences, KAUST, Thuwal 23955-6900, Saudi Arabia

Contents

Supplementary Discussions

Supplementary Figures

Supplementary References

Contents

Supplementary Discussions

Supplementary Discussion 1: Effect of Target-Electrode Interactions on Gate Electrochemical Properties

To verify how gate electrochemical properties change when a biomarker interacts with the electrode surface, we monitored the sensing interface using an electrochemical quartz crystal microbalance (e-QCM-D; Supplementary Fig. 1a).[1,2] The sensing model used in this experiment is a nanobody functionalized gold electrode for the detection of SARS-CoV-2 spike protein.[3] This approach enables real-time monitoring of the resonance-frequency shift of a piezoelectric quartz–gold electrode on which the nanobody was immobilized to capture the target (Supplementary Fig. 1b). The e-QCM-D provides a benchmark validation of binding because its primary signal arises from piezoelectric mass loading rather than electrochemical transduction.[4,5] For a given excitation, the oscillation frequency is highly sensitive to changes in electrode mass, which can vary upon protein adsorption at the surface. The −30 Hz frequency shift observed here confirms protein binding to the recognition layer.

Protein binding can modify the electrode surface potential and dipole distribution through the introduction of additional charges, leading to polarization of the interfacial biolayer.[6–8] Changes in surface potential (or electrochemical potential) can be measured directly using Kelvin probe force microscopy (KPFM),[7,9] or open circuit potential (OCP) measurements,[10,11] or inferred indirectly from electrochemical impedance spectroscopy (EIS).[12] Here, we monitored the electrochemical potential via OCP and measured a −25 mV shift upon target binding (Supplementary Fig. 1c). The electrode double layer capacitance can also change, for example decrease due to formation of a more insulating protein layer or increase if binding disrupts packing within the biolayer and enhances ion accessibility at the interface.[13,14] Such changes can be quantified using EIS or cyclic voltammetry (CV). We report a capacitance decrease of −62 nF extracted from EIS through Randles circuit fitting (Supplementary Fig. 1d). The charge-transfer resistance (R_{CT}) may also vary depending on how target binding alters electrode accessibility to a redox probe in solution,[15] as reflected by the increase in semicircle diameter in the Nyquist plot. We do not investigate the contribution of R_{CT} to the OECT response here as our work focuses on non-redox based, non-Faradic sensing that relies on changes in electrochemical potential and capacitance.[6,16–18]

Contents

Supplementary Discussion 2: Preparation of Model Gate Electrodes with Different Electrochemical Potential and Constant Capacitance

The electrochemical potential of Ag/AgCl reference electrodes containing inner solutions with varying Cl^- concentrations, was measured against a commercial Ag/AgCl reference electrode (3 M NaCl) (Supplementary Fig. 2). The electrochemical potential (E) depends linearly on the log[Cl^-] according to the Nernst equation (Equation S1) and the corresponding electrochemical reaction (Equation S2):[19]

$$E = E^0 - RT/nF \cdot \log[Cl^-] \qquad \text{Equation S1}$$

$$AgCl_{(s)} + e^- \rightleftharpoons Ag_{(s)} + Cl^-_{(aq)} \qquad \text{Equation S2}$$

where E^0 is the standard reduction potential of $AgCl_{(s)}/Ag_{(s)}$ redox couple, R is the universal gas constant, T is temperature in Kelvin, n is the number of electrons involved in the redox reaction, F is the Faraday constant, and [Cl^-] represents the chloride ion concentration used to finely tune the electrode potential.

The range of [Cl^-] selected for the model electrodes (from 3 M to 50 mM) ensured non-polarizable behavior. [Cl^-] below 50 mM led to polarization when the electrode was used as a gate of the OECT. The non-polarizability requirement is not merely a theoretical condition leveraged in this work but is a widely adopted strategy in transistor-based biosensing, through the use of large-area (high capacitance) gates, mainly to maximize biolayer conformational changes upon target binding and minimize sensing time.[8,20] The prepared electrodes exhibited a minimal potential drift (-0.13 ± 0.06 mV/min), comparable to that of a commercial reference electrode (Fig. 2a).[21]

Contents

Supplementary Discussion 3: The Electrochemical Potential–Current-Voltage (EP-IV) Characterization

In this work we used the EP-IV characterization setup (Supplementary Fig. 4a).[22,23] This technique helps understanding the OECT operation by correlating device output signals with electrochemical potential distributions of OECT components.[24] To operate the OECT, we applied V_{DS} (-0.6 V) and V_{GS} (from -0.7 to +0.2 V) using a source measure unit (SMU) while simultaneously monitoring the electrochemical potentials of source (E_S), drain (E_D), and gate (E_G) with respect to a reference electrode (RE) using a potentiostat in open-circuit potential (OCP) mode. The transfer curve recorded during these measurements (Supplementary Fig. 4b) and the potential distributions of OECT components (Supplementary Fig. 4c) can be used for the experiment interpretation. E_G remained constant during the entire scan due to the non-polarizable nature of the Ag/AgCl gate electrode, while the relative electrochemical potentials of the OECT components align with the applied operating voltages, i.e, E_D-E_S = -0.6 V (V_{DS}) and E_G-E_S = -0.7 to +0.2 V (V_{GS}).

Contents

Supplementary Discussion 4: Revisiting the Current Model for OECT based non-Faradaic Biosensor Operation

The conventional model that describes the non-faradaic biosensing mechanism in OECTs (Supplementary Fig. 6a) can be described by the following equations:[18,25,26]

$$V_{GS}{}^{eff} = V_{GS,1} + V_{offset} \quad \text{Equation S3}$$

Boundary conditions:

- Blank $\rightarrow$
$$\begin{cases} V_{GS}{}^{eff} = V_{GS,1} & \text{Equation S4} \\ V_{offset} = 0\ V & \text{Equation S5} \end{cases}$$

- Target $\rightarrow$
$$\begin{cases} V_{GS}{}^{eff} = V_{GS,2} = V_{GS,1} + V_{offset} & \text{Equation S6} \\ V_{offset} = f(\Delta\varphi_G, \Delta C_G) & \text{Equation S7} \end{cases}$$

where $V_{GS}{}^{eff}$ is the effective gating voltage required to reach a set I_{DS} value taken as reference point. $V_{GS,1}$ and $V_{GS,2}$ are the instrumentally applied gating voltages for the blank and target conditions necessary to reach the set I_{DS}. V_{offset} represents the additional gate voltage needed to compensate for changes in gate electrochemical properties following target binding and reach the set I_{DS}. $\Delta\varphi_G$ and ΔC_G are the changes in gate surface potential and capacitance resulting from target binding.

The $V_{GS,1}$ is distributed across the gate–electrolyte and electrolyte–channel interfaces depending on their relative capacitances.[27] The voltage drop across the electrolyte–channel interface determines the I_{DS}. In this model, I_{DS} in the blank condition is taken as the reference point, meaning $V_{GS}{}^{eff} = V_{GS,1}$ and there is no V_{offset} (Equations S4 and S5). Following target binding, the gate electrochemical properties (surface potential, capacitance, or both) change. To maintain the same $V_{GS}{}^{eff}$ and thus the same I_{DS}, a new gate voltage ($V_{GS,2}$) must be applied. The $V_{GS}{}^{eff}$ is now $V_{GS,2}$ which differs from $V_{GS,1}$ by V_{offset} (Equation S6). V_{offset} then depends on the gate property change (Equation S7). As a result, the voltage drop across the gate–electrolyte interface changes, while the drop across the electrolyte–channel interface remains unchanged, preserving the reference doping condition.

The relationship between analyte concentration and the gate electrochemical properties changes is defined by:

$$\Delta\varphi_G = \frac{nQ_{tgt}}{\varepsilon_{tgt}\varepsilon_0} d_{tgt} \quad \text{Equation S8}$$

$$\Delta C_G = \frac{\Delta\varepsilon_r \varepsilon_0 A}{\Delta d} \quad \text{Equation S9}$$

where n is the surface density of bound target molecules, Q_{tgt} is the net charge of a single target molecule (dependent on its isoelectric point, electrolyte pH and ionic strength), ε_0 is the dielectric permittivity of the free space, ε_{tgt} is the relative dielectric permittivity of the target and d_{tgt} is the thickness of the target capable of electrostatically interacting with the gate conductive surface, which depends on the Debye length, $\Delta\varepsilon_r$ is the variation in dielectric permittivity of the gate, A is the gate electroactive area, and Δd is the variation in biolayer thickness.

While this model describes the OECT sensor operation, the way how it is presented has some ambiguities and inaccuracies:

1. **Mislabeled y-axis:** In the conventional model, the y-axis is often labeled as *potential*, even though electrochemical potential refers to the thermodynamic state of an electrode and must be defined relative to a true reference electrode or a well-characterized redox couple.[19] In contrast, *voltage* is the electric potential difference between any two arbitrary points. The channel is fixed at 0 V, effectively serving as the reference for this representation. However, the channel is neither an independent nor a thermodynamically defined reference electrode. Therefore, the y-axis should be labeled as "voltage vs. channel" and it cannot convey meaningful thermodynamic information about OMIEC doping or gate surface potential.
2. **Emphasis on ΔV_{GS} (or V_{offset}) instead of ΔI_{DS}:** The model uses voltage shift ($\Delta V_{GS} = V_{offset}$) as sensor output, rather than current response (ΔI_{DS}). The channel is assumed to maintain a constant voltage drop relative to the electrolyte, i.e., constant I_{DS}, with the effect of sensing being considered only as a variation of the voltage drop across the gate-electrolyte interface.

However, this perspective overlooks the core function of the OECT which is a voltage-to-current transducer and ΔI_{DS} is the amplified sensor output.

3. **Undefined contributions to V_{offset}:** In the current model, it is not possible to quantify how much of the V_{offset} is due to gate capacitance or surface potential variation, or both ($V_{offset} = f(\Delta C_G, \Delta\varphi_G)$), Supplementary Fig. 6a.
4. **Apparent gate capacitance change:** The model always suggests a change in the capacitance of the gate electrode after target binding even when the sensing response is solely related to variations of surface potential ($V_{offset} = f(\Delta\varphi_G)$). See the increase in voltage drop across gate-electrolyte interface which suggest a decrease in gate electrode capacitance (Supplementary Fig. 6b).
5. **Incompatibility with non-polarizable gate electrodes:** The model constrains the channel and electrolyte potentials at fixed values. However, when working with a low polarizable gate (which can be obtained using an electrode of large area),[8,22] the voltage drop across the gate-electrolyte interface is negligible before and after target binding,[28] and the only source of signal is a change in surface potential ($V_{offset} = f(\Delta\varphi_G)$). However, the only possible representation is an apparent increase in the gate–electrolyte voltage drop, which contradicts the non-polarizable nature of the gate (Supplementary Fig. 6c).

The revised description of the model proposed in this work addresses the inaccuracies and ambiguities outlined above and it also introduces new elements that enhance our understanding of sensor operation. By expressing the y-axis as voltage relative to a true reference electrode (e.g., Ag/AgCl), the model provides thermodynamically meaningful values. These voltages correspond to well-defined electrochemical potentials that govern both the OMIEC doping state and the gate surface potential, enabling a more rigorous and informative interpretation.

Below is a summary of key advantages of this approach:

1. **Representation of real experimental practices:** OECT sensors are often operated by monitoring changes in I_{DS} through transfer curves. The revised representation reflects this operating mode by describing the device at a fixed V_{DS} and a V_{GS} range rather than relying on the less intuitive concept of voltage compensation (V_{offset}) to maintain a constant I_{DS} after target binding.

2. **Direct link to classical potentiometric sensing:** The revised representation establishes a direct conceptual and experimental bridge to classical potentiometric sensing techniques, such as the OCP method (Figs. 2a and 2b) by reporting the actual electrochemical potential of the gate electrode. This connection facilitates cross-validation and interpretation across sensing platforms.
3. **Correlation with broader electrochemical characterization of the OMIEC:** The revised representation enables direct correlation between the OECT response and other electrochemical characterizations of the OMIEC such as cyclic voltammetry (CV), electrochemical impedance spectroscopy (EIS), and conductivity measurement (Fig. 2d). This gives access to a mechanistic understanding of how the OECT transduces target binding events into an amplified current signal.[29]
4. **Mapping of the electrochemical potential gradients across the channel:** By including the applied V_{DS} in the schematic, the model clearly illustrates the electrochemical potential distribution along the channel.[24] This enables the identification of whether the OECT is operating within safe electrochemical voltage range (Supplementary Fig. 7a).[30,31] For example, if V_{DS} is too negative (Supplementary Fig. 7b) or V_{GS} is too positive (Supplementary Fig. 7c-i), the potential at the drain may reach values capable of degrading the OMIEC.[32] Conversely, excessively negative V_{GS} values can push the source to potentials that promote overoxidation of the OMIEC[33] (Supplementary Fig. 7c-ii). Such effects can lead to a change in I_{DS}, which may be falsely attributed to a sensing response if not properly identified. Therefore, mapping the potential landscape ensures both accurate interpretation and safe operation of the device.

Contents

Supplementary Discussion 5: Distinguishing applied voltage from electrochemical potential

We reported the EP-IV characterization obtained during a linear voltage scan of an Au electrode in a solution containing the redox probe $[Ru(NH_3)_6]Cl_3$ (Supplementary Fig. 10a). The measurement was performed using the EP-IV setup (Supplementary Fig. 4) adapted for a two-electrode configuration (Supplementary Fig. 10a-i). The experiment was repeated using two non-polarizable electrodes of different materials connected to the (−) lead (denoted $(-)_1$ and $(-)_2$), while the electrode connected to the (+) lead was kept constant.

During the voltage scan, the Ru(II)→Ru(III) oxidation occurs in both cases, but at different applied voltages (Supplementary Fig. 10a-ii), separated by 31 mV (ΔV_p). When the curve obtained with $(-)_2$ is shifted horizontally by ΔV_p, it overlaps with the $(-)_1$ curve ($(-)_2 + \Delta V_p$, dashed line), analogous to the behavior observed in OECT transfer curves (Fig. 2b-i).

The origin of this effect becomes clear when the electrochemical potentials of the (+) and (−) electrodes are simultaneously measured versus a reference electrode (Ag/AgCl in 3 M NaCl) during the voltage scan (Supplementary Fig. 10a-iii). The potentials of the two (−) electrodes differ by a constant offset of 31 mV ($\Delta E_{(-)}$), matching the horizontal shift observed in the I_{Au} trace. Likewise, the (+) potential traces are vertically offset by the same amount, consistent with the behavior observed for the OECT (Fig. 2b-ii).

This analysis highlights the fundamental distinction between applied voltage and electrochemical potential. Drawing two vertical lines at the voltages corresponding to the Ru oxidation peak for the two (−) electrodes shows that both intersect the (+) electrochemical-potential trace at the same value (Supplementary Fig. 10a-iii). Thus, the voltage applied by the SMU represent only the electrical potential difference between two arbitrary points—here, the (+) and (−) electrodes—and, by itself, has no thermodynamic meaning. In contrast, the electrochemical potential has thermodynamic significance: in both (−) cases, the Ru oxidation peak occurs at the same electrochemical potential. Specifically, the electrochemical potential measured by the potentiostat corresponds to the potential difference between the electrode under investigation and a reference electrode whose potential is stable, well defined, and governed by the Nernst equation. As a result, the Ru oxidation peak may appear at different applied voltages depending on the specific two-electrode configuration, but it is thermodynamically associated with a unique electrochemical potential.

An analogous concept applies to OECT operation: while a given I_{DS} can be obtained at different applied V_{GS}, depending on gate properties (Fig. 3a-i), the same I_{DS} corresponds to a specific and unique OMIEC doping state.

A similar analogy explains the non-uniform transfer-curve shift observed upon variation of gate capacitance. In this case, an analogous experimental setup was employed, with the (+) electrode fixed and the capacitance of the (−) electrode varied (Supplementary Fig. 10b-i). Specifically, the (−) electrode capacitance decreased from a High-C condition (low-polarizability electrode) to a Low-C condition (high-polarizability electrode) by reducing the electrode area (Supplementary Fig. 10b-ii). Decreasing the (−) electrode capacitance produced a pronounced but non-uniform shift in the I_{Au} trace; consistent with the behavior observed in OECT transfer curves (Fig. 4b). Simultaneous measurements of electrode electrochemical potentials reveal that, under low-capacitance conditions, the (−) electrode no longer maintains a constant potential but instead exhibits a bias-dependent deviation due to polarization (Supplementary Fig. 10b-iii). This effect propagates to the (+) electrode, such that at a given applied voltage, different electrochemical potentials are reached, mirroring the behavior observed in OECTs (Fig. 4c).

The polarization of the low-capacitance (−) electrode can be quantified at each applied bias as V_{drop}. When the I_{Au} trace measured under Low-C conditions is corrected by subtracting the corresponding V_{drop} at each voltage, it collapses onto the High-C curve, demonstrating that the same electrochemical potential, or redox state, was reached despite different applied voltages.

Contents

Supplementary Discussion 6: Modulation of Channel Capacitance During OECT Operation

Since we measured the electrochemical potentials that the channel experienced during a transfer curve using EP-IV, we can now estimate the channel capacitance at each of these potentials through independent EIS measurements (Supplementary Fig. 12a). PEDOT:PSS capacitance increased when the channel was pushed toward more negative potentials (i.e., positive V_{GS}), suggesting a variable C_G/C_{CH} depending on the OECT operational voltage.

According to Bernards model,[27,34] V_{drop} is a function of the gate-to-channel capacitance ratio (C_G/C_{CH}) (Equation S10):

$$V_{drop} = \frac{1}{1+\frac{C_G}{C_{CH}}} V_{GS} \qquad \text{Equation S10}$$

The effect of variable C_G/C_{CH} can be observed also during the OECT operation since the V_{drop}/V_{GS} depends exclusively on the C_G/C_{CH}. We calculated the V_{drop}/V_{GS} during transfer curve measurements for 19 gate electrodes with different capacitances (Supplementary Fig. 12b). The V_{drop}/V_{GS} for all devices results not constant, i.e., C_G/C_{CH} is not constant, and displayed a highly reproducible dependence on the doping voltage, in line with the trend in the PEDOT:PSS capacitance vs. V_{GS}. These results validate the voltage-dependent nature of the of C_G/C_{CH} and highlight the need to consider this variable C_G/C_{CH} when interpreting OECT sensing response.

Supplementary Discussion 7: Interpolation of Expected Output Values

We previously obtained a correlation between gate capacitance (C_G) and gate polarization (V_{drop}) at each applied V_{GS} (Supplementary Fig. 11). This calibration enables extraction of empirical relationships describing this dependence and, in turn, prediction of the expected OECT output current (I_{DS}) from the specific gate input parameters (C_G and E_G) and their variations.

To perform this analysis, the OECT response must first be calibrated using a reference gate electrode so that the OMIEC doping state can be expressed in thermodynamic units (i.e., electrochemical potentials). Accordingly, an initial characterization step was carried out using an Ag/AgCl pellet electrode. The electrochemical potential of this electrode is reproducible and can also be calculated via the Nernst equation based on the electrolyte composition. Under these conditions, the doping voltage can be reported as V_{GS} (V vs Ag/AgCl), emphasizing the thermodynamic relevance of the applied voltages (Supplementary Fig. 13a). This calibration allows voltages applied with a given gate to be converted into thermodynamic values that can be directly associated with the measured I_{DS}.

For a PEDOT:PSS OECT, the transfer curve can be empirically approximated by a quadratic expression:

$$I_{DS} = B_0 + B_1 \cdot V_{GS,eff} + B_2 \cdot V_{GS,eff}^2 \qquad \text{Equation S11}$$

Where B_0, B_1 and B_2 are the fitted coefficients (-1.46E-2 A, 3.84E-2 A/V and 2.65 A/V2, respectively), and $V_{GS,eff}$ is the effective gate voltage which depends on the electrochemical properties of the gate.

The effective gate voltage is calculated by accounting for (i) the difference between the gate electrochemical potential and the reference condition of Ag/AgCl pellet (first term) and (ii) the additional shift in effective doping voltage induced by gate polarization (second term), according to:

$$V_{GS,eff} = V_{GS} - \left(E_G - E_{G,ref}\right) - (D_0 + D \cdot V_{GS}) \qquad \text{Equation S12}$$

where V_{GS} is the instrumental gate bias applied using the gate electrode under test, E_G is the electrochemical potential of the gate, $E_{G,ref}$ is the electrochemical potential of the reference gate

(Ag/AgCl pellet, 50 mV vs Ag/AgCl 3M in 1x PBS), D_0 and D are coefficients from the linear relationship that links V_{drop}, V_{GS} and gate capacitance (Supplementary Fig. 11a).

Finally, the dependence of V_{drop} on gate capacitance is required. As previously shown (Supplementary Fig. 11c), the linear coefficients D_0 and D vary exponentially with $\log C_G$, following:

$$D_0 = y_i + A_i exp - (logC_G - x_i)/t_i \quad \text{Equation S13}$$

$$D = y_s + A_s exp - (logC_G - x_s)/t_s \quad \text{Equation S14}$$

where y_i, A_i, x_i and t_i are the fit parameters describing the intercept D_0 (2.43E-3 V, 9.688E-2 V, -7.2202 and 3.95E-1, respectively), and y_s, A_s, x_s and t_s are the fit parameters describing the slope D (5.38E-3 V, 2.512E-1 V, -7.2170 and 3.44E-1, respectively).

Together, these empirical relationships allow prediction of the expected OECT output for a gate electrode with defined electrochemical properties (E_G and C_G). As an illustrative example, we report three cases of gate electrodes with different properties, within the range of variations induced by target binding, and compare the measured transfer curves with the corresponding calculated curves, showing that the prediction error remains within an acceptable range lower than 5%, (Supplementary Fig. 13b-d).

These equations enable exploration of hypothetical scenarios involving variations in gate electrochemical properties, thereby facilitating sensing optimization, for example, with respect to bias selection for extracting I_{DS}, initial gate size, and the direction of electrochemical property changes. This approach is relevant when the resulting calibration can be transferred to a batch of devices with comparable performance, provided that the channels are identical. Importantly, this calibration is not intended to be performed on every OECT channel used for sensing, as it requires extensive device operation that may induce degradation.

Supplementary Discussion 8: Gate Size Range for Maximum Sensitivity to Capacitance Changes

As experimentally demonstrated, OECT sensitivity to changes in gate capacitance improves by decreasing the gate size (Fig. 5b-ii); however, it is crucial to use a gate whose capacitance (C_G) is larger than the channel capacitance (C_{CH}). If C_G becomes smaller than C_{CH}, an excessive portion of V_{GS} will drop across the gate–electrolyte interface (i.e., V_{drop}), rather than being transmitted to the channel, preventing an efficient OMIEC modulation (Equation S10 and Supplementary Fig. 14a).[27] To ensure effective channel modulation and optimal sensing conditions, a C_G/C_{CH} between 1 and 10, highlighted as region of interest (ROI), is required, as it allows for more than 50% of V_{GS} to drop on the channel.

If we define n as C_G/C_{CH}, and α as the relative change in gate capacitance upon target binding ($\alpha = C_G^*/C_G$, where C_G is the gate capacitance before target binding, and C_G^* after), the ΔV_{drop} caused by the sensing event can now be expressed using the Bernards model as follows:

$$\Delta V_{drop} = \frac{n(1-\alpha)}{(1+\alpha n)(n+1)} V_{GS} \qquad \text{Equation S15}$$

The ROI conditions appear to correspond also to the highest OECT sensitivity, i.e., highest ΔV_{drop} due to gate capacitance changes (C_G^*/C_G), as a function of the C_G/C_{CH} (Equation S15 and Supplementary Fig. 14b-i). For example, assuming that C_G^*/C_G is 10% upon target binding,[1] ΔV_{drop} increases as C_G/C_{CH} approaches 1 (Supplementary Fig. 14b-ii). However, when C_G/C_{CH} drops below 1, ΔV_{drop} begins to decline, establishing this value as the lowest limit for gate size optimization.

Supplementary Discussion 9: Quantification of the Combined Electrochemical Potential and Capacitance Effect on the OECT Response

To investigate the combined contributions of changes in gate electrochemical potential and capacitance to the OECT response, we applied the EP-IV analysis under conditions in which the gate electrode undergoes both types of changes (Supplementary Fig. 15). In the example shown here, the gate potential increased by 53 mV and the capacitance decreased by 69 nF, consistent with realistic sensing conditions.[1,25] The transfer curves using the Blank and Target gates were measured (Supplementary Fig. 15a-i; the corresponding changes in gate electrochemical properties are annotated within the plot to highlight the parameters driving the OECT response). The potentials of the two gate electrodes are analyzed under two conditions: (1) prior to applying any external bias ("no V"), and (2) during transfer-curve acquisition (Supplementary Fig. 15a-ii). The "no V" condition displays the variation of gate electrochemical potential (ΔE_G) upon target binding. The influence of the capacitance change, manifested as different degrees of electrode polarization at the OECT terminals, arises only when operating voltages are applied during transfer curve measurements. Under bias, the two gates polarize to different extents because of their different capacitances. These two polarization conditions, denoted V^B_{drop} and V^T_{drop}, are indicated, for example, at $V_{GS} = 0$ V. As expected, the higher capacitance of the Blank gate results in lower polarization ($V^B_{drop} < V^T_{drop}$). By calculating the difference between the two polarization values at each specific V_{GS}, ($\Delta V_{drop} = V^T_{drop} - V^B_{drop}$), we quantify the binding-induced change in gate polarization as a function of operating bias. Subtracting ΔV_{drop} from the Target traces ($V_{GS,\,target} - \Delta V_{drop}$ and $E_{G,\,target} - \Delta V_{drop}$) effectively removes the contribution of the capacitance change. The resulting transfer curve retains only the effect of ΔE_G (Supplementary Fig. 15b-i), and the Target gate exhibits the same polarizability as the Blank gate (Supplementary Fig. 15b-ii). In this capacitance-compensated representation, the residual offset between $E_{G,\,blank}$ and $E_{G,\,target}$ equals the ΔE_G measured under "no V" conditions and remains constant across the full V_{GS} range, consistent with the case of isolated gate potential variations. If ΔE_G is also subtracted from the corrected Target traces ($V_{GS,\,target} - \Delta V_{drop} - \Delta E_G$ and $E_{G,\,target} - \Delta V_{drop} - \Delta E_G$), the Blank and Target traces overlap (Supplementary Figs. 15c-i, ii), indicating that both gate potential and capacitance contributions have been removed. This behavior mirrors what was observed previously (Figs. 2b-i and 4b) and confirms that, once all changes in gate electrochemical properties (potential and capacitance) are accounted for, the OECT responses becomes identical. The input signals can be

expressed under a unified voltage term, ΔV_{input}, since both manifest in the form of voltage, and can be reported as function of V_{GS} (Supplementary Fig.15c-iii). This representation is consistent with the individual analyses of gate potential and capacitance effects (Fig. 2b-ii and Supplementary Fig. 11a, respectively).

In this experiment, simultaneous changes in both parameters were realized using two gold electrodes of different areas. While capacitance can be conveniently tuned by adjusting gate size, the gate potential is hardly controllable even for electrodes made of the same material because it depends on multiple factors.[35,36] Consequently, systematically sampling the full space of possible ΔE_G and ΔC_G combinations is non-trivial. Nevertheless, this limitation does not preclude investigation of the OECT sensing transduction mechanism: representative single cases, such as the example reported above, are consistent with the trends established in the preceding analyses and support the conclusions drawn.

Supplementary Discussion 10: Assessment of OECT stability during successive transfer curve acquisition

To ensure that the channel current is stable during a sensing protocol that involves successive transfer curve acquisition, a control measurement can be integrated. The OECT channel is first characterized using an Ag/AgCl gate within a previously identified safe voltage window; this serves as the reference measurement (Ref. IV, Supplementary Fig. 20). After each sensing measurement (e.g., each concentration used to build a calibration curve), the channel is re-characterized under identical conditions (C_n Check, Supplementary Fig. 20). Each control measurement is then compared to the initial reference to quantify the relative current loss, ΔI_{DS} (%), which should remain below a predefined threshold (e.g., <5%). We reported an example of a progressive I_{DS} loss following successive sensing steps, with substantial degradation already evident at the third measurement (C_2) (Supplementary Fig. 20). This is further confirmed by the failure of the EP-IV curve-shifting procedure to achieve overlap after compensating for the change in gate electrochemical potential (ΔE_{WE}), indicating that the observed response is dominated by parasitic effects. This protocol enables both assessment of OMIEC stability and selective exclusion of unreliable data. For instance, only the initial experiments (Blank and C_1) satisfy the stability criterion (ΔI_{DS}<5%), whereas subsequent measurements must be discarded. By contrast, in a stable sensing experiment Ag/AgCl control measurements consistently showed ΔI_{DS} below 5%; and the EP-IV analysis yields near-perfect overlap of the transfer curves after compensating for the gate-potential variation (Supplementary Fig. 21). All sensing data points in this case can therefore be considered reliable.

Supplementary Figures

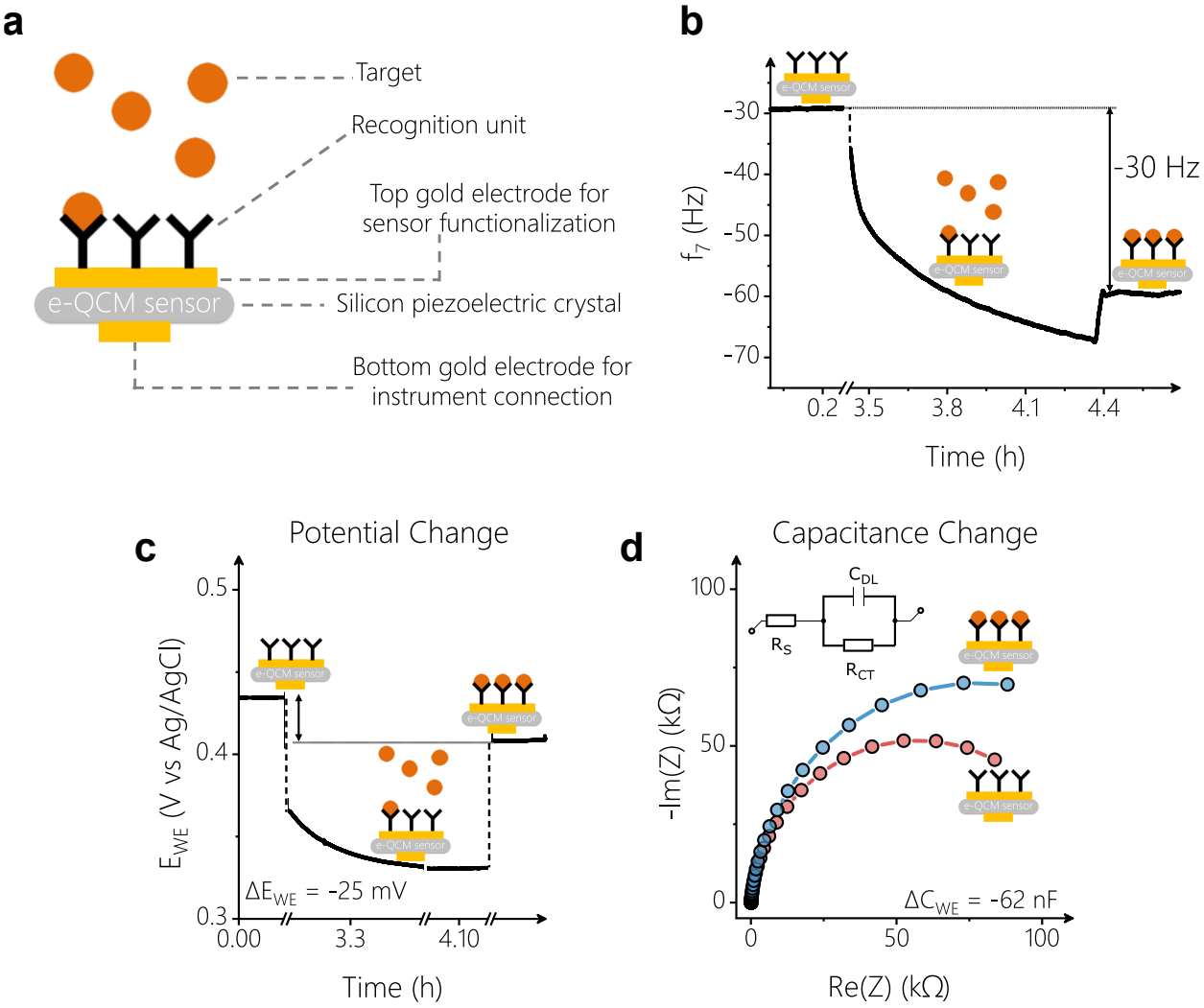

Supplementary Figure 1. Effect of target-electrode interactions on gate electrochemical properties. a) Schematic of the e-QCM-D sensor architecture. **b)** Resonance-frequency shift (7th overtone) of the crystal during binding of SARS-CoV-2 spike protein to the immobilized nanobody. The initial phase corresponds to the electrode in buffer (blank); the middle phase corresponds to exposure to buffer containing 1 nM target (incubation); and the final phase corresponds to rinsing with target-free buffer to remove unbound species, leaving only specifically bound protein (washing). **c)** Simultaneous measurement of the e-QCM-D electrode's open-circuit potential (electrochemical potential). **d)** Nyquist plot of the nanobody-functionalized electrode before and after target binding measured using electrochemical impedance spectroscopy (EIS). The electrode double layer capacitance was obtained by fitting the curve to the Randles equivalent circuit shown in the inset.

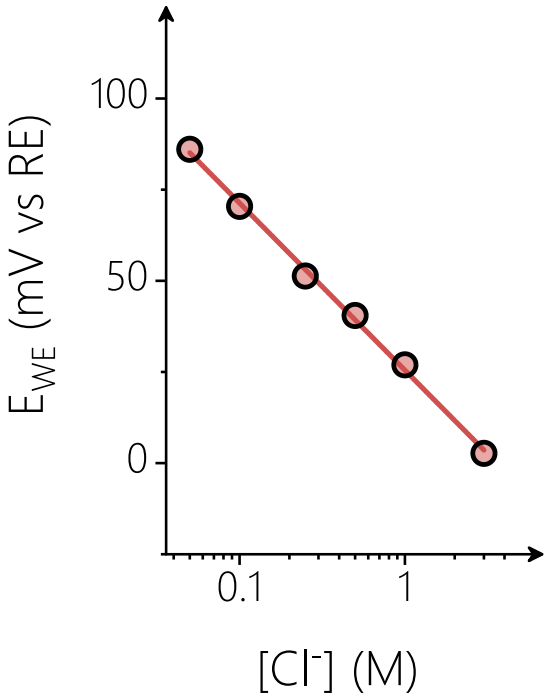

Supplementary Figure 2. Electrochemical potential of Ag/AgCl electrodes. The electrodes contain inner solutions with varying Cl^- concentrations from 3 M to 50 mM, measured against a commercial Ag/AgCl reference electrode (3 M NaCl).

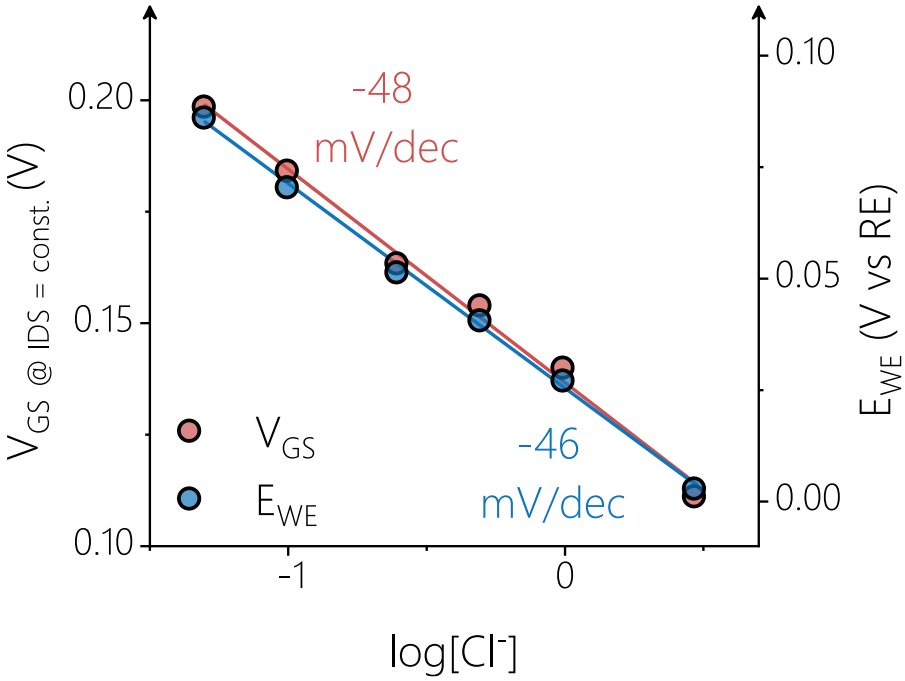

Supplementary Figure 3. V_{GS} generating the same channel current and gate electrode potential with respect to Cl^- concentrations. The potential of the gate electrodes and the shift of the transfer curves have an identical dependence on the [Cl^-] concentration of the inner solution of the Ag/AgCl electrode.

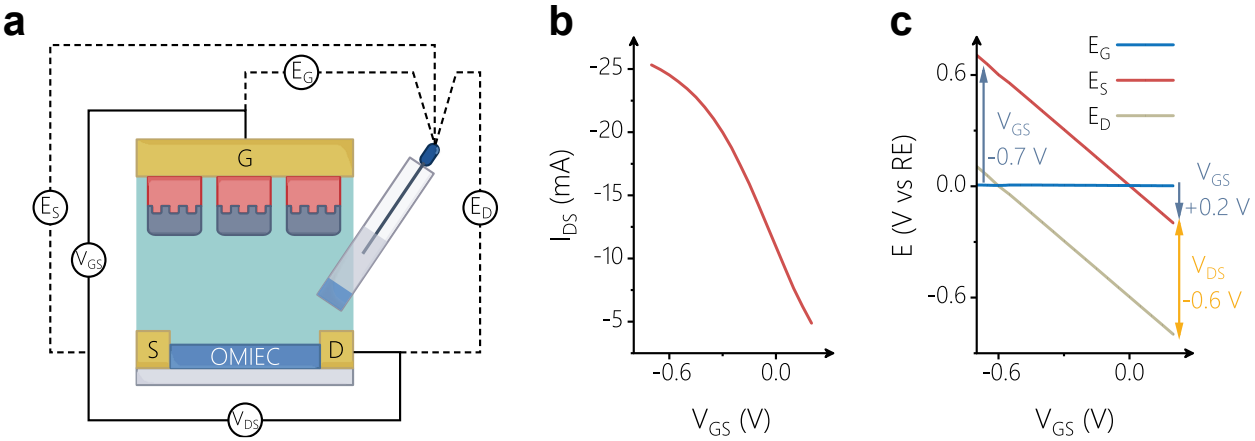

Supplementary Figure 4. EP-IV setup and measurement. a) Experimental setup for the simultaneous application of V_{DS} and V_{GS} to the OECT using a source measure unit (SMU), and independent measurements of E_S, E_D and E_G using a potentiostat and a reference electrode (RE). Dashed lines indicate the electrical connections to the potentiostat, while solid lines represent those to the SMU. **b)** Transfer curve. **c)** Electrochemical potentials of the OECT components during the transfer curve.

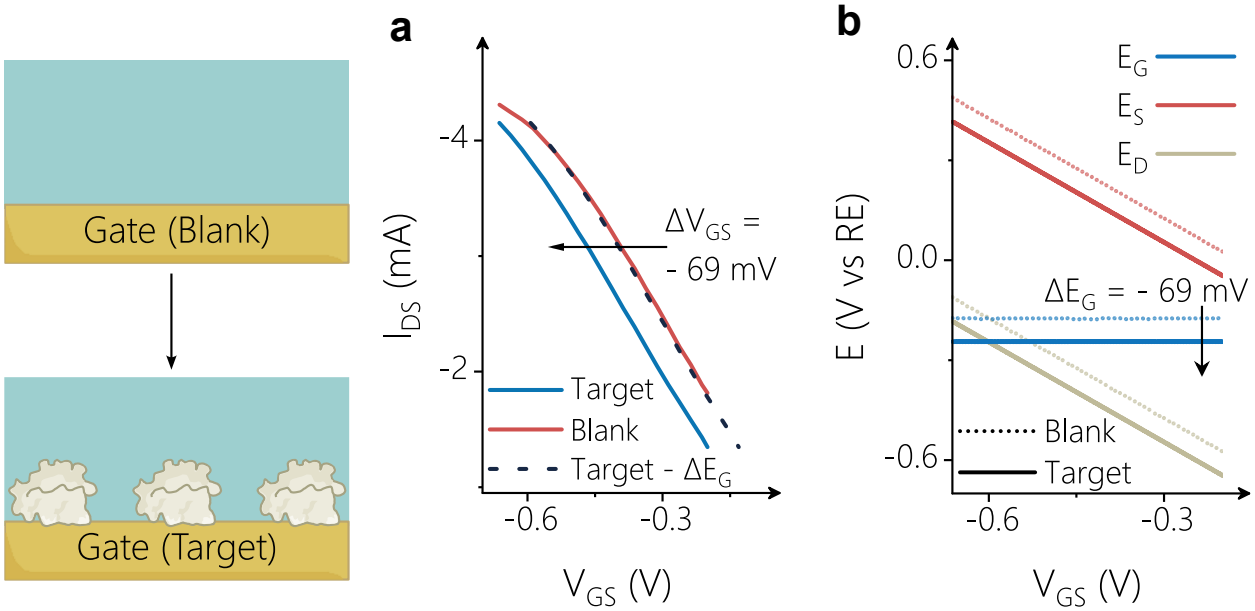

Supplementary Figure 5. Effect of protein-induced gate electrochemical potential changes on OECT output. PEDOT:PSS gate incubated with bovine serum albumin (BSA) and corresponding OECT measurement performed in 1 mM phosphate buffer. **a)** Transfer curves recorded before (blank) and after (target) BSA binding at the gate; the black dashed trace corresponds to the target-bound curve shifted horizontally by 69 mV. **b)** Corresponding electrochemical potentials of gate (E_G), source (E_S) and drain (E_D); dotted lines indicate the blank-gate condition and solid lines represent the potentials after BSA binding.

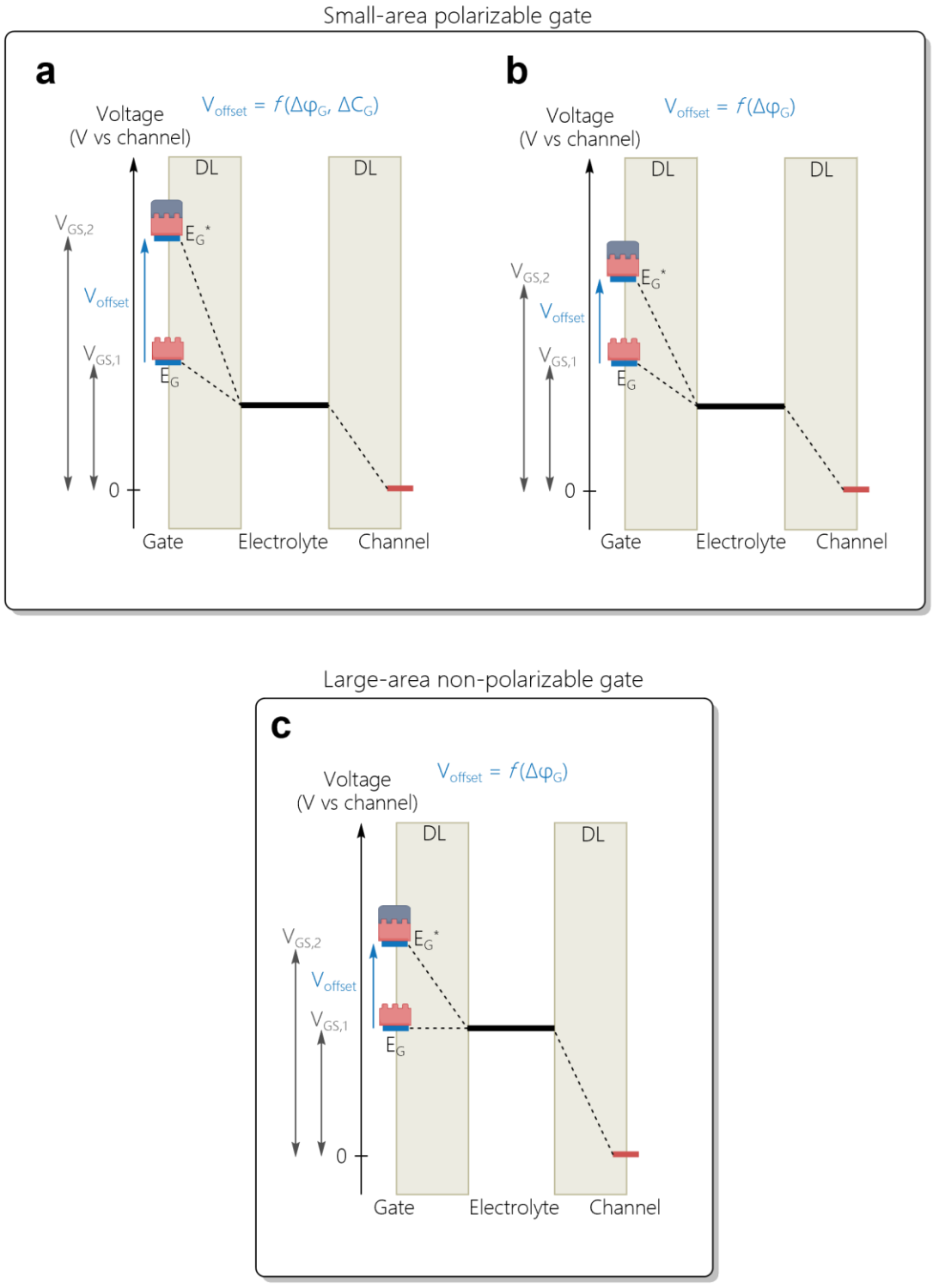

Supplementary Figure 6. Schematic representation of the conventional OECT sensing model. A polarizable gate electrode undergoes **a)** simultaneous changes in electrochemical potential ($\Delta\varphi_G$) and capacitance (ΔC_G) upon target binding or **b)** only a change in electrochemical potential. **c)** A non-polarizable gate exhibits a shift in electrochemical potential, with no voltage drop across the gate–electrolyte interface, despite the apparent representation in the model.

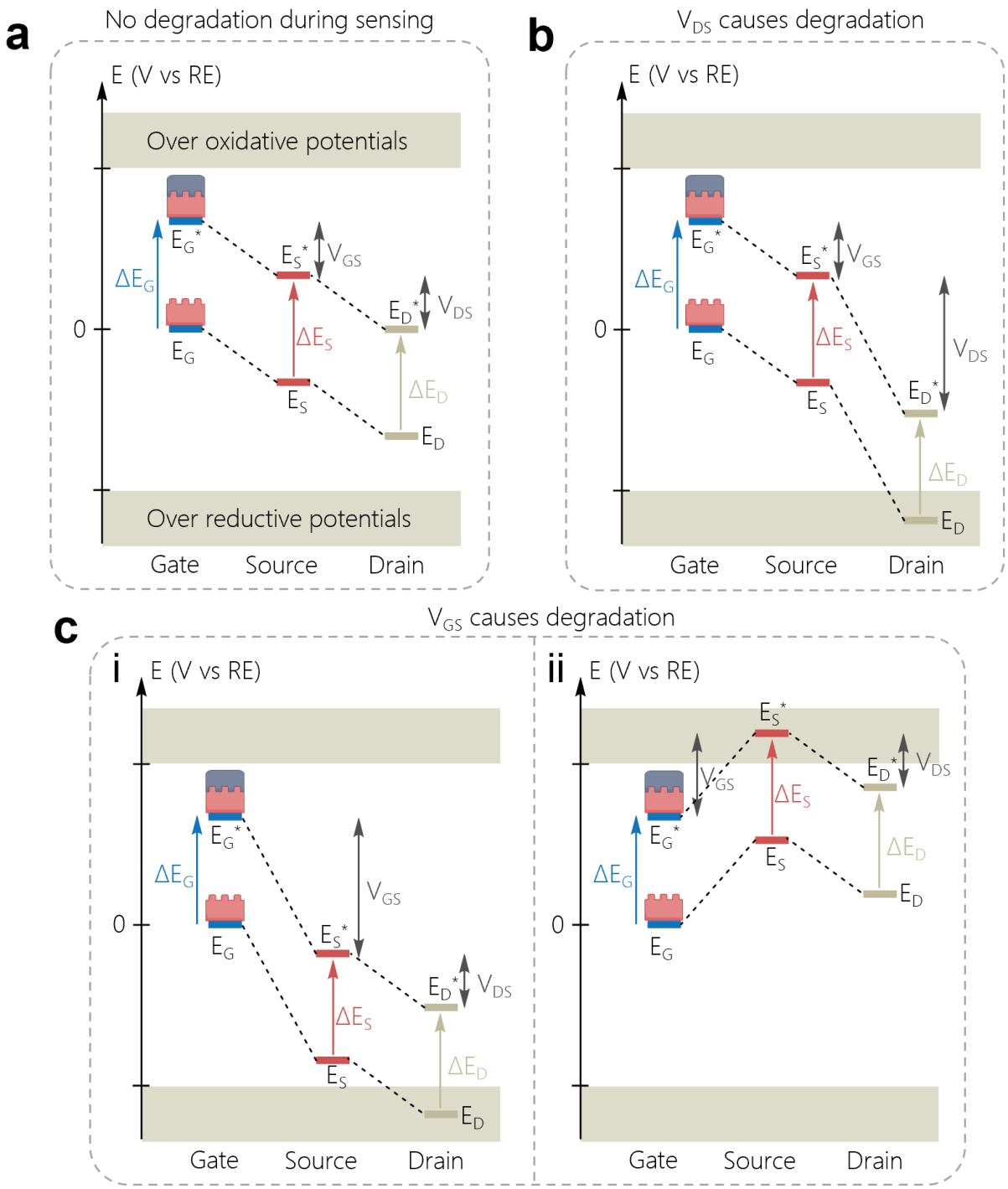

Supplementary Figure 7. Illustration of possible degradation mechanisms under different biasing conditions. a) The OECT operates within a safe voltage window. **b)** Degradation of the OMIEC occurs due to an excessively negative V_{DS}. **c)** Degradation caused by **(i)** an excessively positive, or **(ii)** an excessively negative V_{GS}.

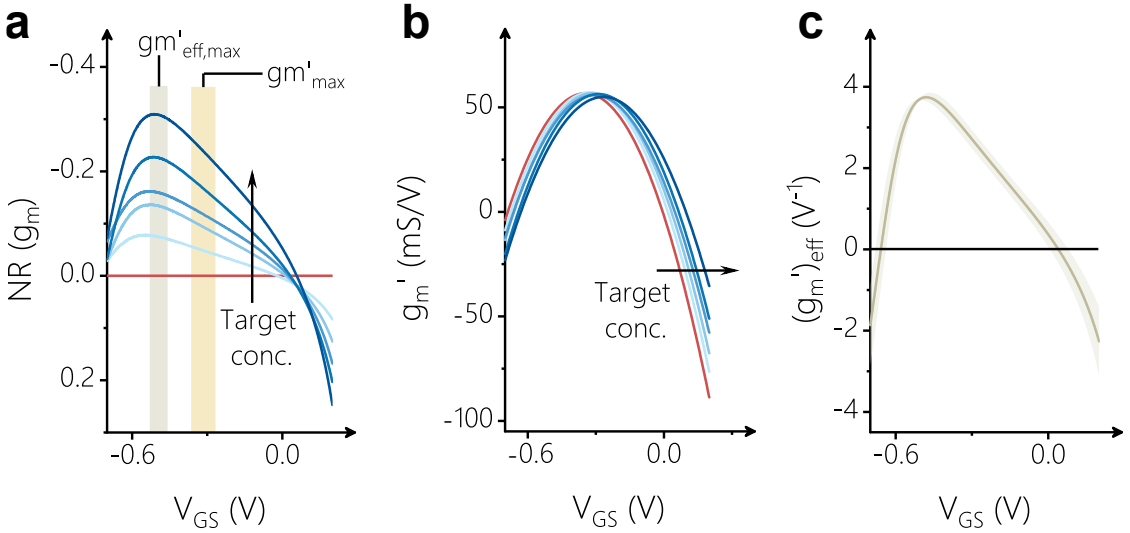

Supplementary Figure 8. Signal efficiency when transconductance is used as the analytical signal. a) Normalized variation of the OECT transconductance derived from the curves shown in Fig. 3a-ii. The derivative of the g_m curves (g_m') maximized at around -0.32 V and the efficiency of g_m curves $(g_m')_{eff}$ maximized at around - 0.49 V. The OECT signal response is maximized at the V_{GS} that maximizes its efficiency. **b)** The g_m' and **c)** $(g_m')_{eff}$ derived from the curves shown in Fig. 3a-ii. $(g_m')_{eff}$ was calculated by averaging the signal efficiency across the sensing gates as function of V_{GS}. The shaded area represents the standard deviation (n=6).

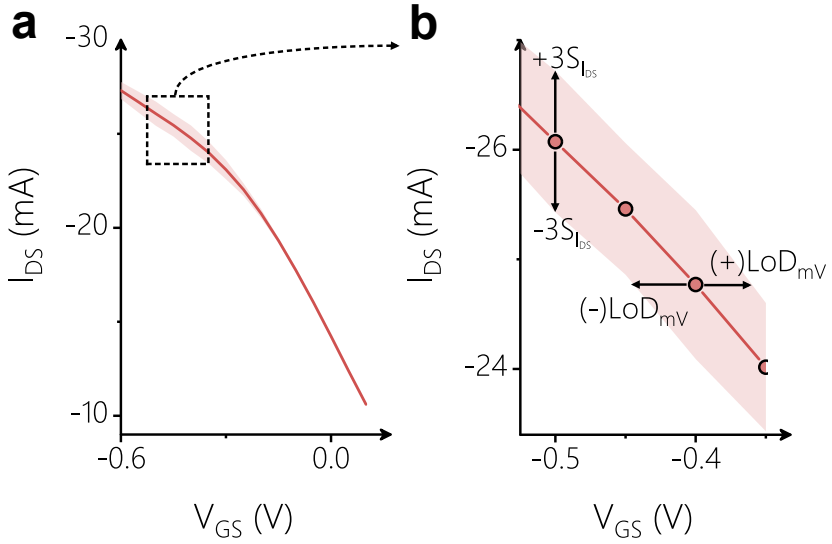

Supplementary Figure 9. Noise associated with the PEDOT:PSS OECT transfer curve measurement. **a)** Representative transfer curve; the shaded region denotes ± 3× the standard deviation (S_{blk}) of the measurement (n = 3), while the plain line represents the mean. **b)** The $\pm 3S_{blk}$ band at each I_{DS} value defines the transfer-curve noise envelope. The corresponding width from the I_{DS} along the V_{GS} axis represents the minimum change in gate potential (ΔE_G) required to shift the transfer curve beyond the noise region. Since $(+)LoD_{mV}$ and $(-)LoD_{mV}$ are similar in absolute value, the limit of detection can be reported as their average magnitude, independent of the shift direction ($|LoD_{mV}|$). Because of the one-to-one correspondence between ΔE_G and ΔV_{GS}, $|LoD_{mV}| = LoD_{\Delta EG}$.

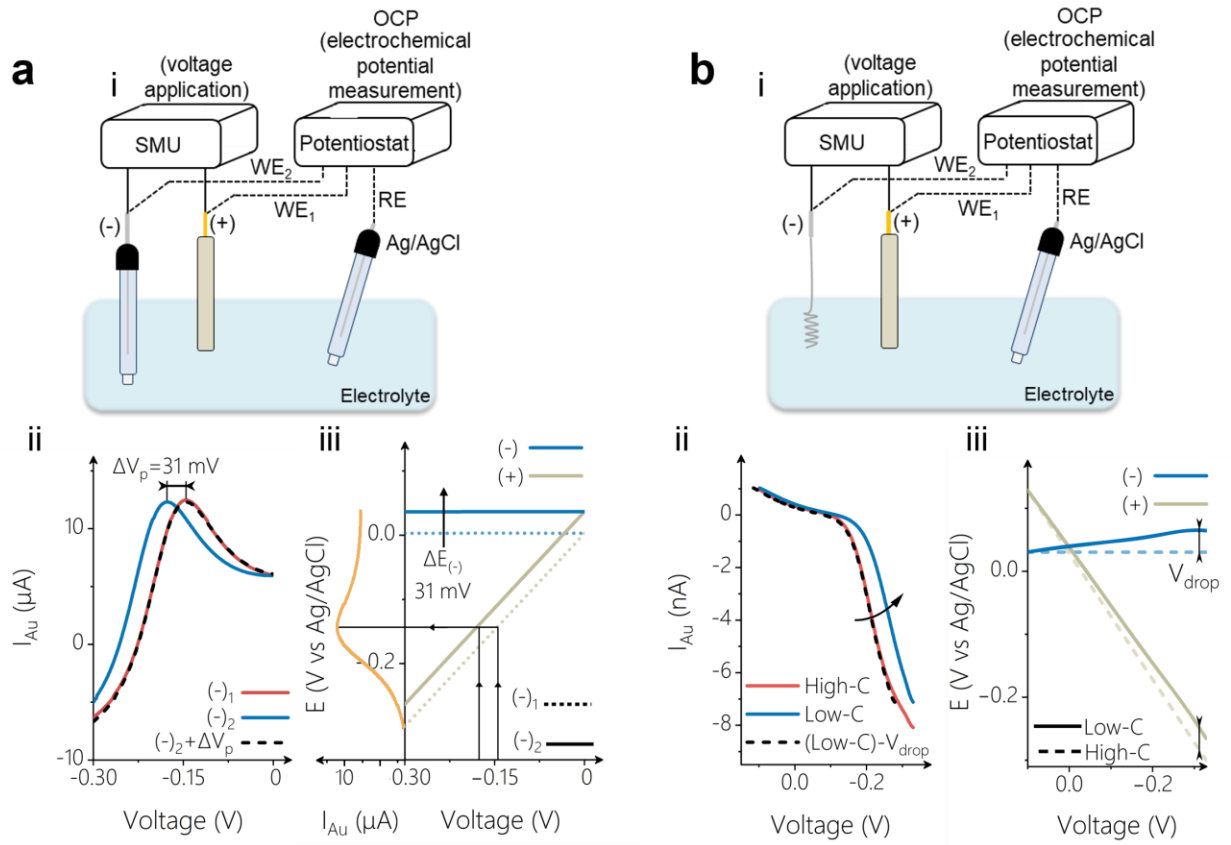

Supplementary Figure 10. Distinguishing applied voltage from electrochemical potential. a) Linear voltage scan coupled with electrochemical potential measurements in a two-electrode configuration. The (−) electrodes used had different potentials while the (+) electrode was the same in all experiments. Schematic of the experimental setup (**i**), current recorded as a function of the applied voltage (**ii**), and electrochemical potentials of the (+) and (−) electrodes during the scan (**iii**). **b)** The same measurement, this time using (−) electrodes of different capacitances. Schematic of the experimental setup (**i**), current recorded as a function of the applied voltage (**ii**), and electrochemical potentials of the (+) and (−) electrodes during the scan (**iii**).

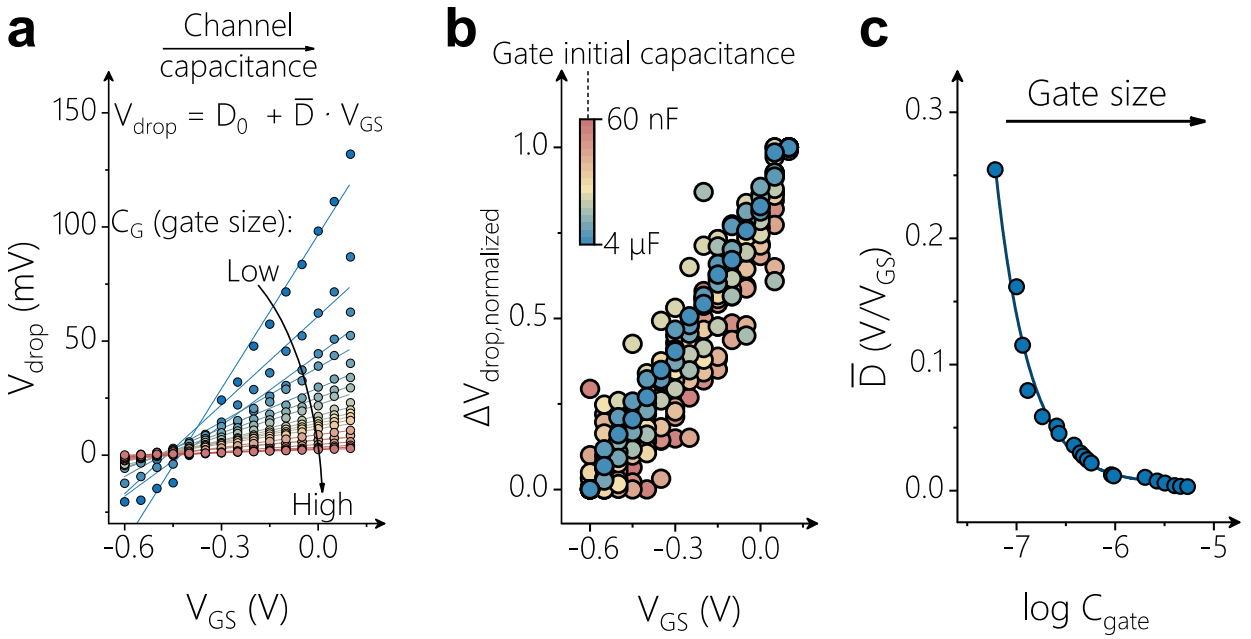

Supplementary Figure 11. Gate polarization dependency on V_{GS} and electrode size. a) Gate electrode polarization (V_{drop}) for gates of different capacitances, ranging from 60 nF to 4000 nF, as a function of V_{GS}. As V_{GS} increased from negative to positive values, the channel capacitance increased. For each gate electrode, the dependency of V_{drop} on V_{GS} is approximated by a linear equation, with intercept D_0 and slope $\bar{D}$. **b)** Normalized ΔV_{drop} as a function of V_{GS} for various initial gate capacitances (indicated by the color scale) and randomly selected ΔC_G upon sensing, ranging from 15 nF to 900 nF. Data extracted from Supplementary Fig. 11a. **c)** Dependence of the slope magnitude, $\bar{D}$, of the linear fits on the gate size. Data extracted from Supplementary Fig. 11a.

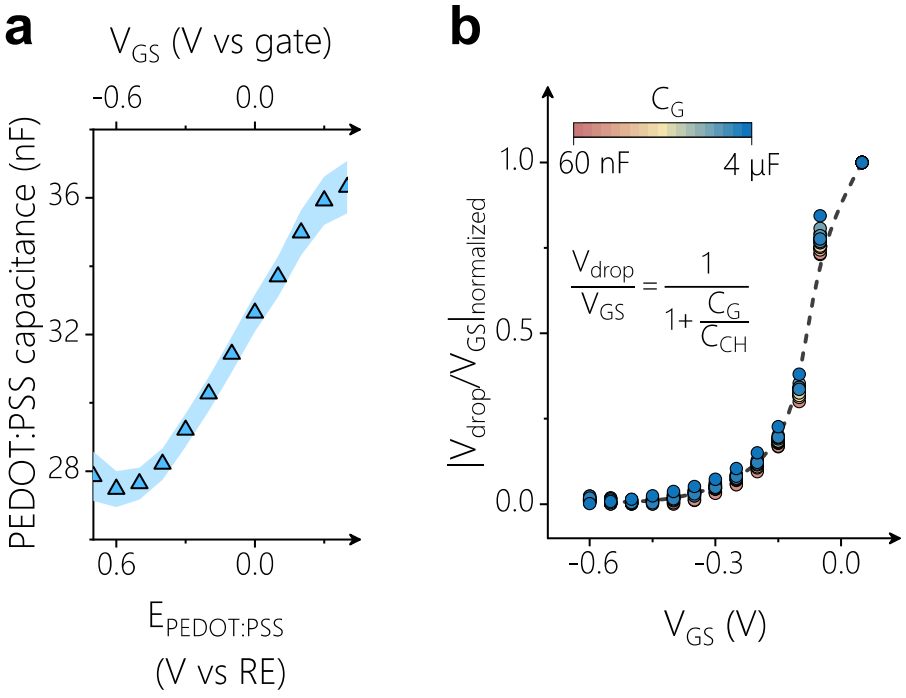

Supplementary Figure 12. Modulation of channel capacitance during OECT operation. a) Capacitance of PEDOT:PSS as a function of electrochemical potential, measured by electrochemical impedance spectroscopy (EIS) and extracted using a Randles equivalent circuit model. **b)** Normalized V_{drop}/V_{GS} values for 19 gate electrodes with capacitances ranging from 60 nF to 4 µF, plotted as a function of V_{GS}. The V_{drop}/V_G depends on the C_G/C_{CH} as indicated by the inset equation. Data were taken from Supplementary Fig. 11a and normalized to 1 with respect to the individual maximum for each curve.

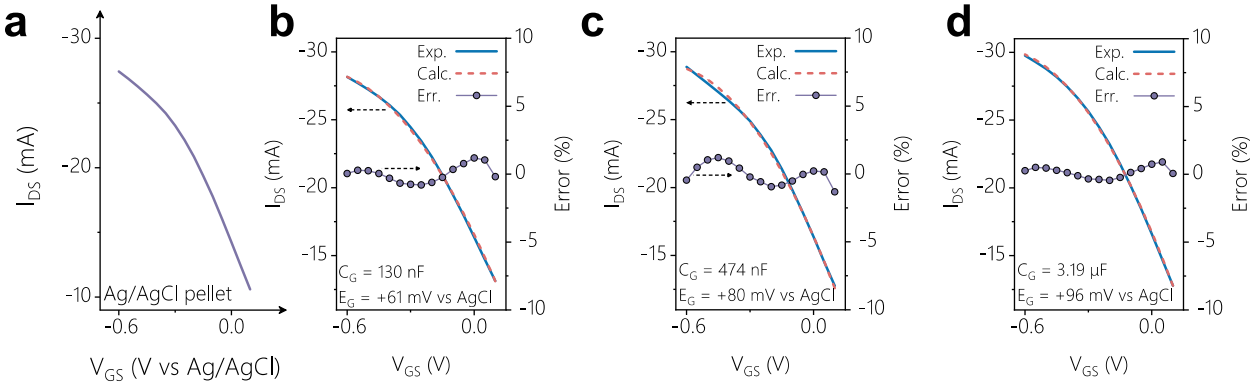

Supplementary Fig. 13. Interpolation of expected output values. a) Transfer curve of a PEDOT:PSS OECT using a reference Ag/AgCl pellet gate electrode to estimate the output current (I_{DS}) at each thermodynamic voltage (electrochemical potential, V vs Ag/AgCl). **b-d)** Representative transfer curves measured using Au gate electrodes with different electrochemical potentials and capacitances, compared with the curves generated using Equation S11. The right y-axis reports the percent difference between the experimental and calculated values. The electrochemical potential and capacitance of each gate electrode are indicated in the corresponding panel.

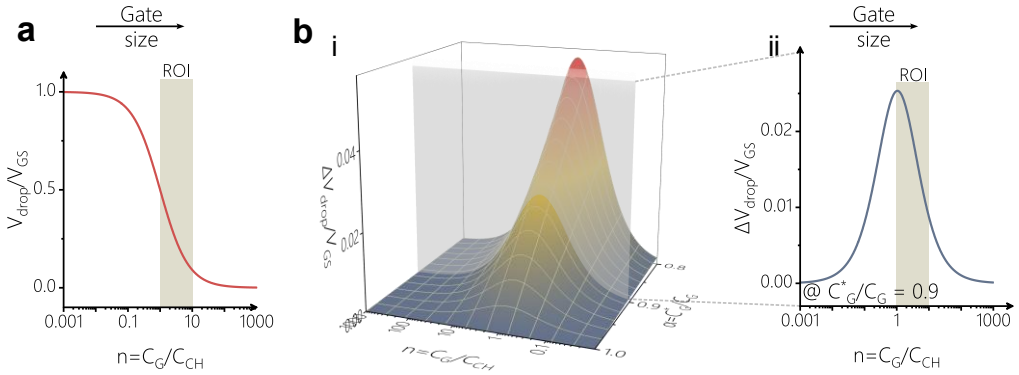

Supplementary Figure 14. Gate size optimal range for maximum sensitivity to capacitance. **a)** Fraction of V_{GS} that drops on the gate, as a function of C_G/C_{CH}. **b)** Dependence of the OECT sensing input signal (ΔV_{drop}) on the C_G/C_{CH}, and C_G^*/C_G (**i**). Specific case illustrating the effect of a 10% gate capacitance change on the ΔV_{drop} as a function of C_G/C_{CH}, (**ii**).

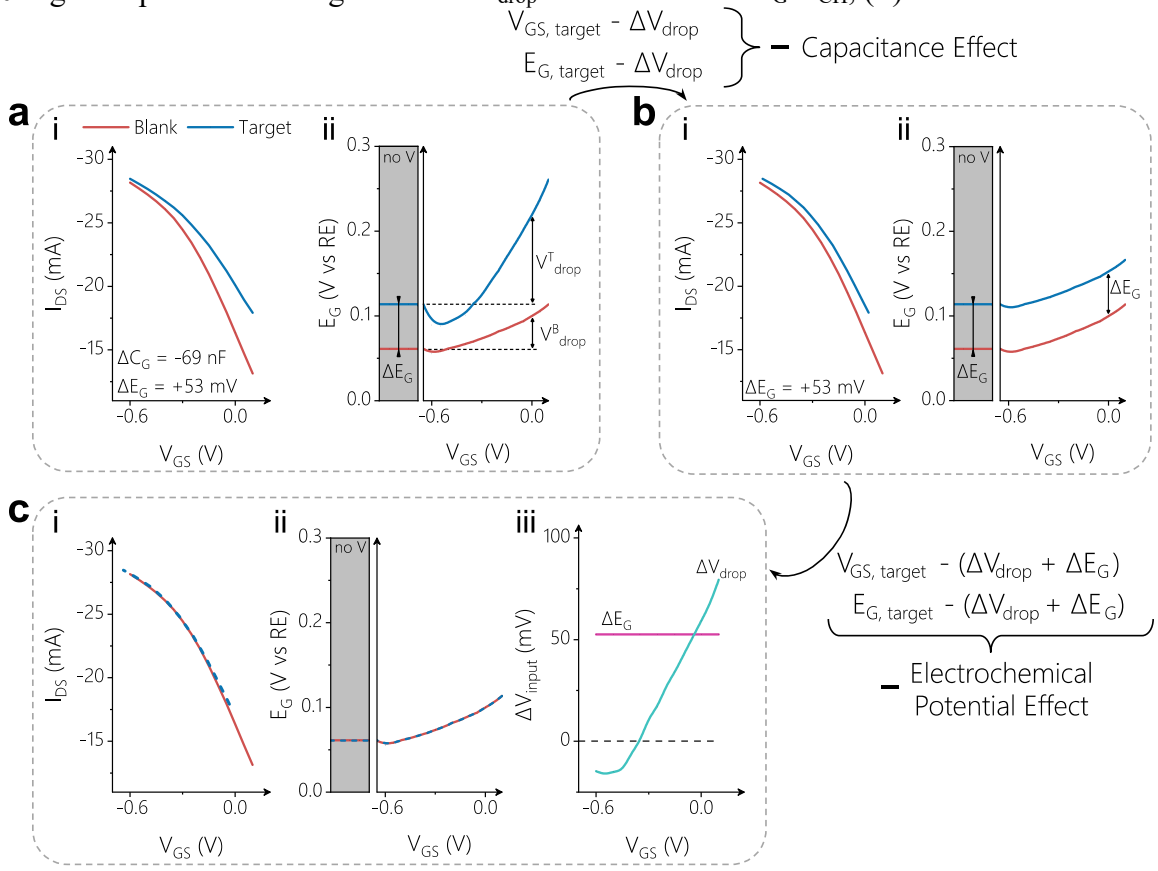

Supplementary Figure 15. EP-IV analysis in which both gate electrochemical potential and capacitance change upon target binding. **a)** Raw data obtained from EP-IV characterization, where (**i**) shows the transfer curves recorded under *Blank* and *Target* conditions, and (**ii**) represents the gate electrochemical potentials measured before applying any bias (no V) and during the transfer curve acquisition. **b)** Data corrected by subtracting the measured gate polarization (V^B_{drop} and V^T_{drop}) from the transfer curves and the electrochemical potential profiles. **c)** Further correction of the *Target* data by subtracting the remaining electrochemical potential difference (ΔE_G) between *Blank* and *Target* conditions.

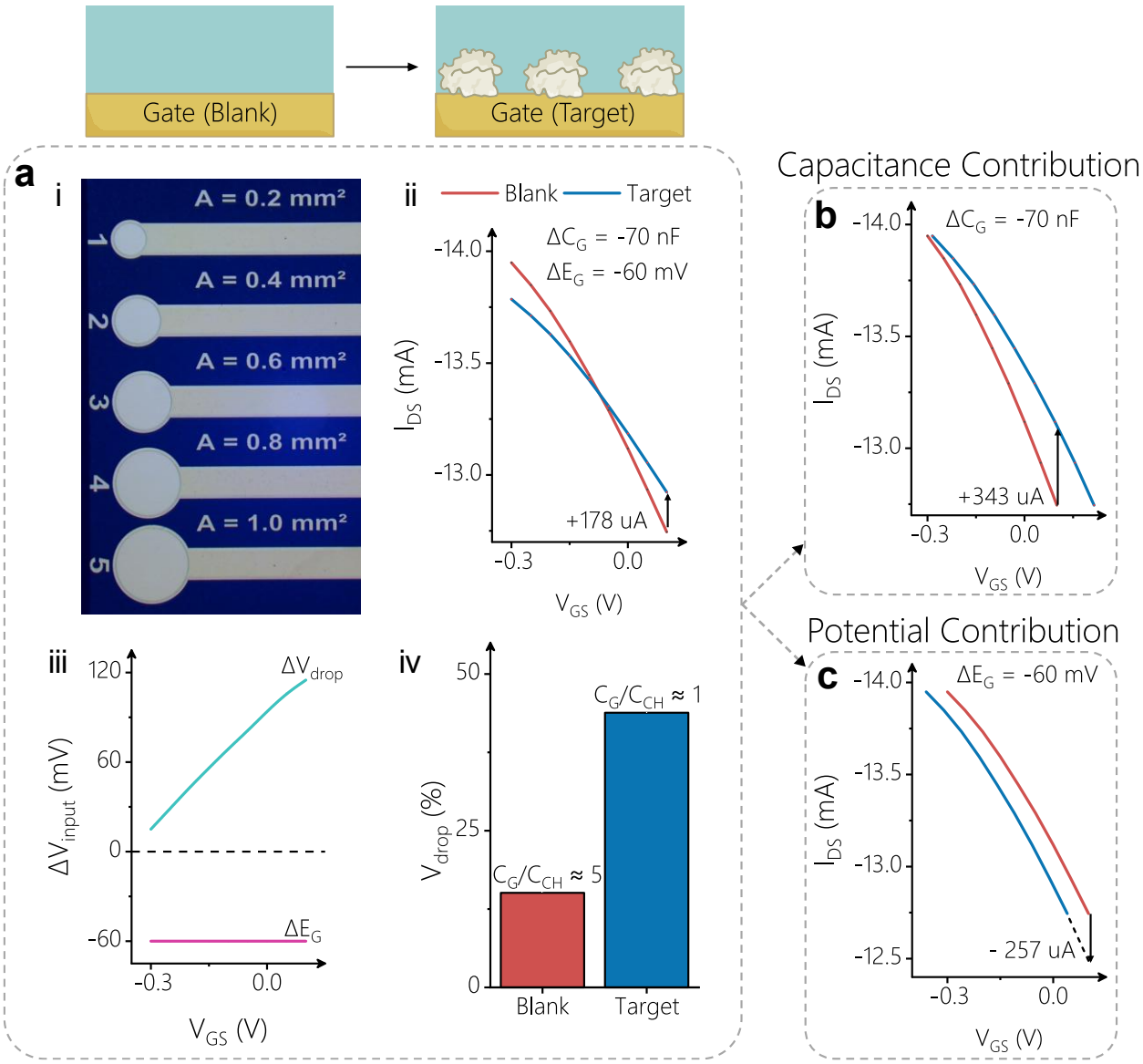

Supplementary Figure 16. Effect of protein-induced changes in gate electrochemical potential and capacitance on OECT output under destructive interaction. a) Gate substrates with varies sizes were used to identify, via EP-IV analysis, the gate area that, when interfaced with the OECT channel, yielded appreciable gate polarization (**i**). Transfer curves acquired in 1 mM phosphate buffer using a 1 mm^2 gold gate before and after incubation with BSA 0.5 wt% (**ii**). ΔV_{input} values extracted by EP-IV analysis following the protocol described in Supplementary Discussion 9. The dashed line separates the regions in which ΔV_{input} shifts the transfer curve toward more positive or more negative V_{GS} (**iii**). Average percentage V_{GS} drop across the gate during the transfer-curve measurement, extracted using the EP-IV analysis and correlated with measured gate and channel capacitances to verify Equation S10 (**iv**). Based on the extracted ΔV_{input} values, calculated hypothetical target transfer curves for the cases of **b)** an exclusive gate-capacitance change and **c)** an exclusive gate-potential change.

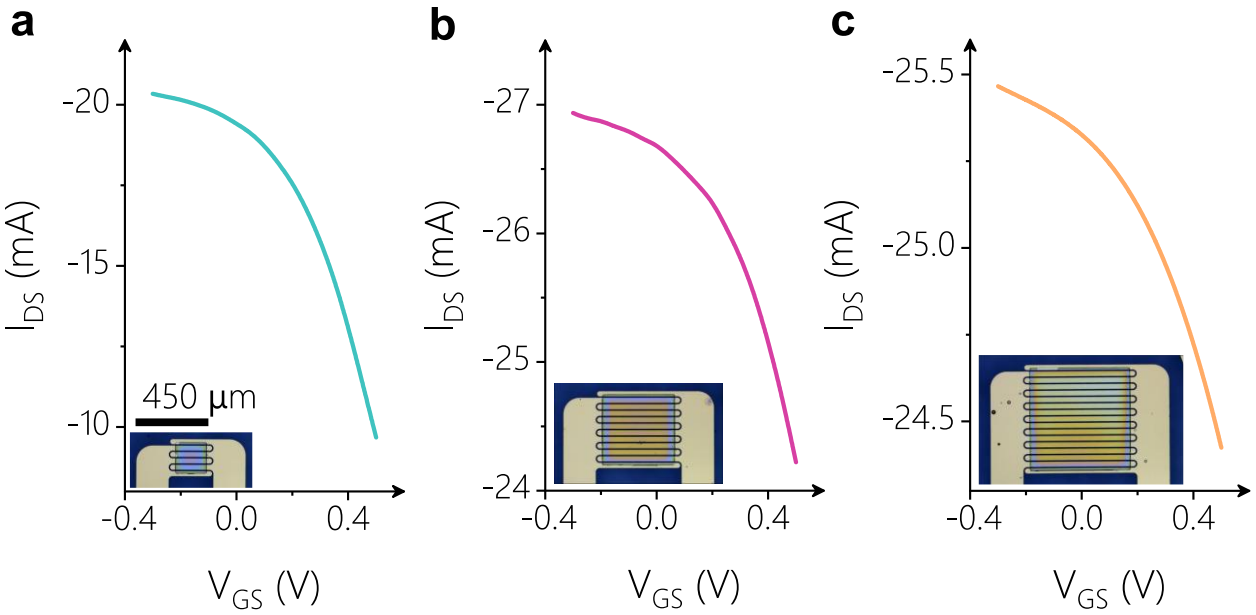

Supplementary Figure 17. Transfer curves of PEDOT:PSS OECTs with different channel dimensions gated by the same polarizable Au electrode (5 mm diameter). Channel dimensions: 200×200 µm (**a**), 450×450 µm (**b**) and 625×625 µm (**c**). The corresponding C_G/C_{CH} ratios are 12.8, 3.4, and 2, respectively. The micrographs in each panel show the OECT channels.

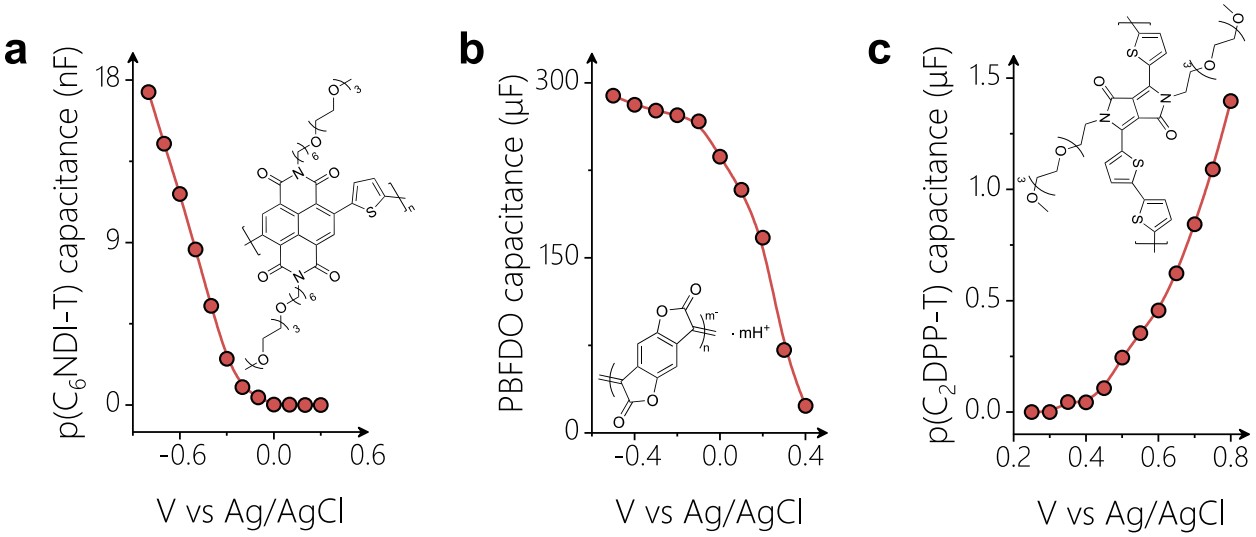

Supplementary Figure 18. OMIEC capacitance as function of doping potential. Capacitance of (**a**) p(C_6NDI-T), (**b**) PBFDO, and (**c**) p(C_2DPP-T) measured at different electrochemical potentials.

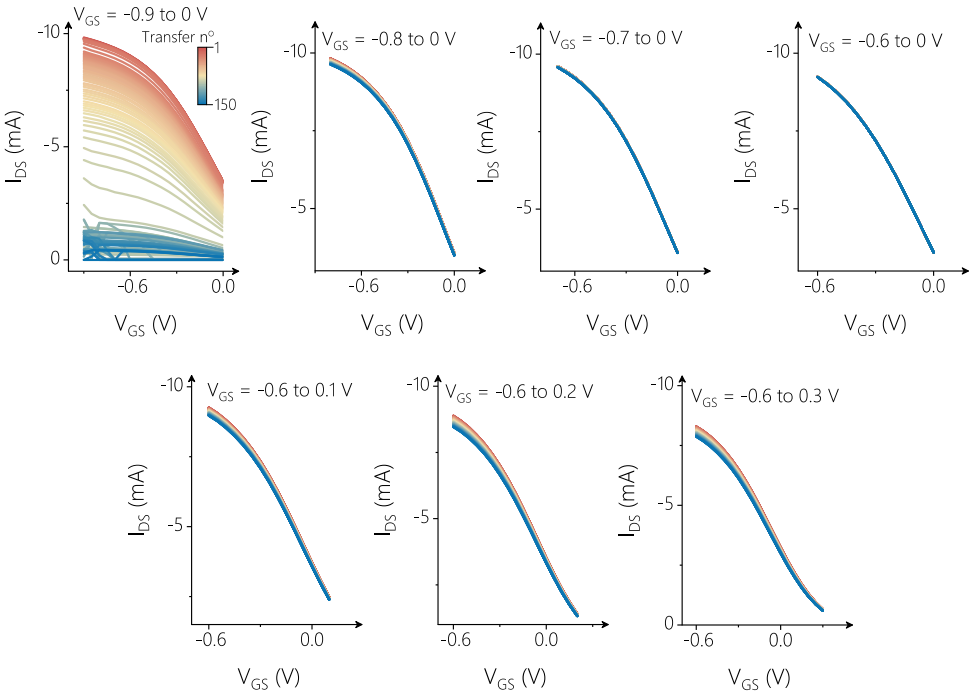

Supplementary Figure 19. Transfer curves acquired during the protocol used to identify the stable V_{GS} operating window reported in Fig. 8b.

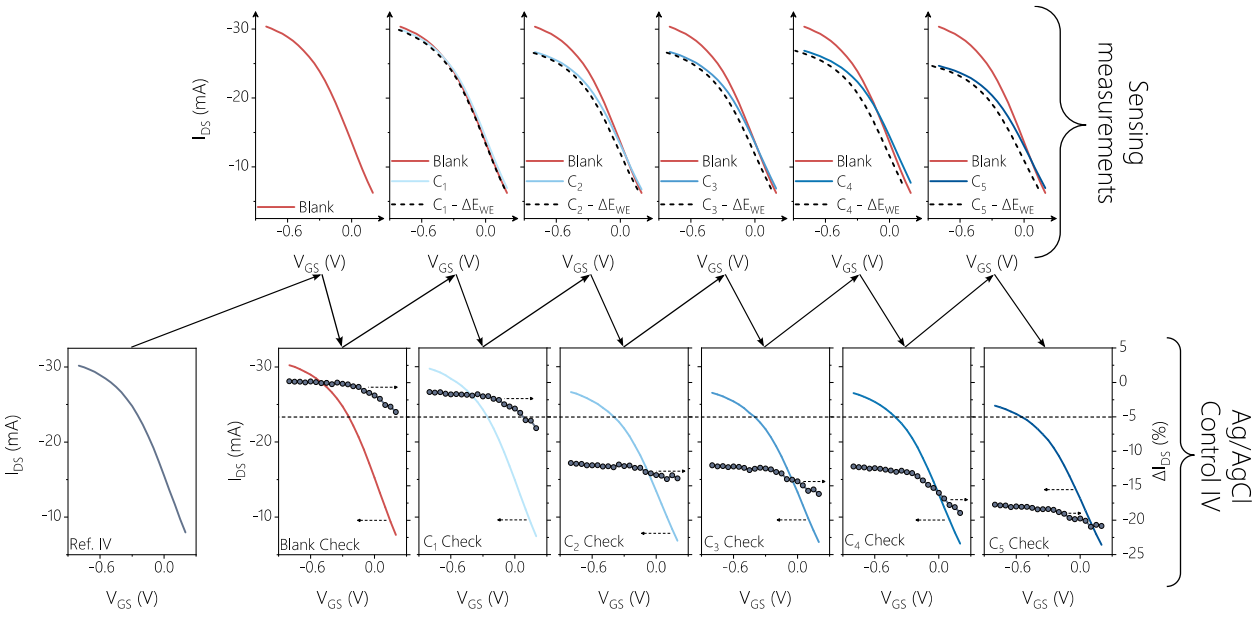

Supplementary Figure 20. OECT sensing measurements in which the gate electrochemical potential changes progressively (top row), together with control measurements with Ag/AgCl gate performed in parallel to assess channel stability (bottom row). The arrows show the sequence of the measurements. The control measurements reveal a progressive loss of I_{DS} over the course of the experiments, which prevents the EP-IV analysis from providing a correct interpretation of the sensing mechanism.

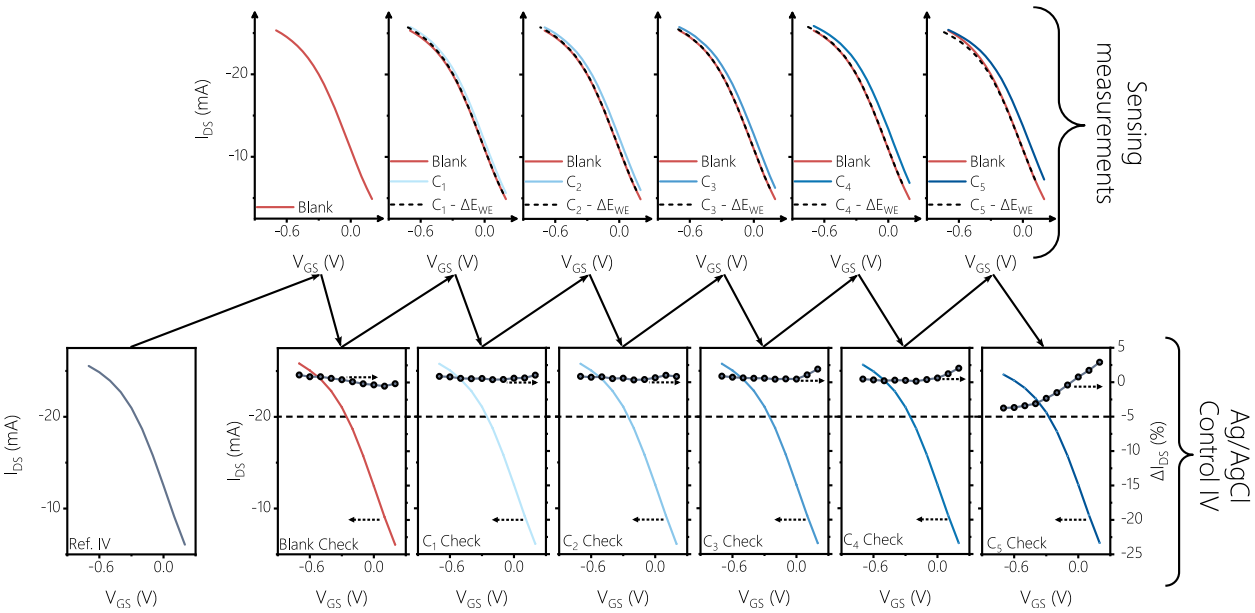

Supplementary Figure 21. Experiment analogous to Supplementary Fig. 20 but performed under conditions where channel current is stable, allowing the EP-IV analysis to provide a correct interpretation of the sensing mechanism. Analysis corresponding to the data reported in Fig. 3a–c.

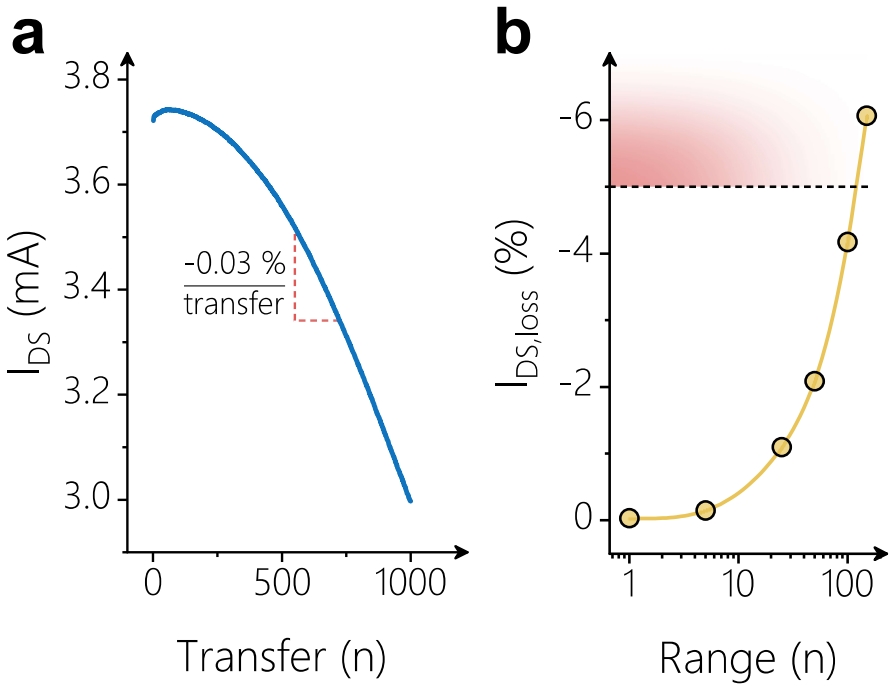

Supplementary Figure 22. OECT channel stability. (**a**) The decrease in I_{DS} (at a fixed V_{GS}) during 1000 consecutive transfer curves. (**b**) Corresponding relative I_{DS} loss during long-term operation as a function of the measurement-range protocol.

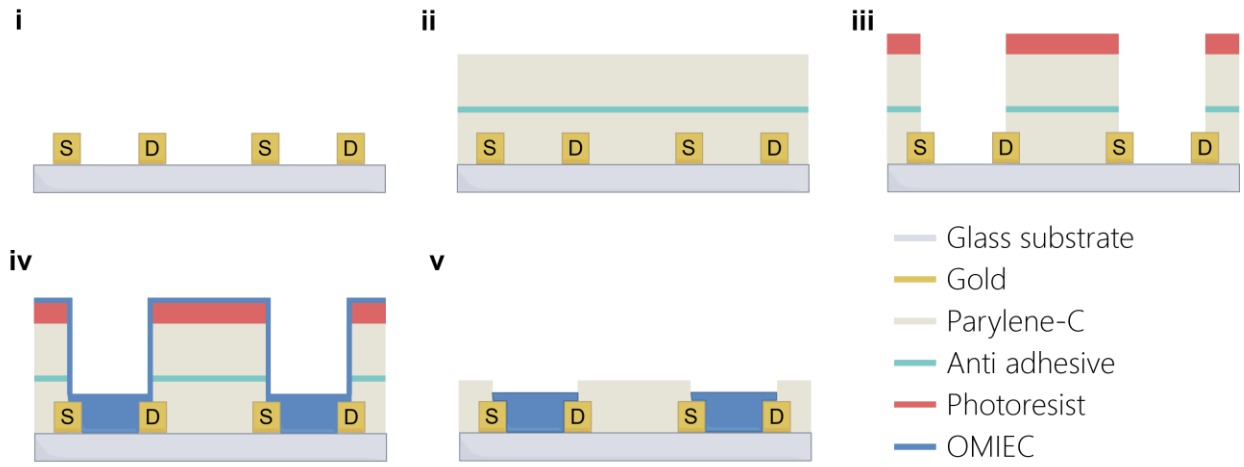

Supplementary Figure 23. OECT fabrication protocol. Schematic of the fabrication workflow of two OECT channels, including source (S) and drain (D) patterning (**i**); deposition of two Parylene-C insulating layers separated by an anti-adhesive layer (**ii**); patterning of the insulating stack and definition of the channel area via photoresist lithography followed by plasma etching (**iii**); OMIEC spin-coating (**iv**); and peel-off of the sacrificial layer (**v**).

Supplementary References

1. Koklu, A. *et al.* Convection Driven Ultrarapid Protein Detection via Nanobody-Functionalized Organic Electrochemical Transistors. *Advanced Materials* **34**, (2022).
2. Ohayon, D. *et al.* Interactions of Catalytic Enzymes with n-Type Polymers for High-Performance Metabolite Sensors. *ACS Appl. Mater. Interfaces* **15**, 9726–9739 (2023).
3. Guo, K. *et al.* Rapid single-molecule detection of COVID-19 and MERS antigens via nanobody-functionalized organic electrochemical transistors. *Nat. Biomed. Eng.* **5**, 666–677 (2021).
4. Qiao, X., Zhang, X., Tian, Y. & Meng, Y. Progresses on the theory and application of quartz crystal microbalance. *Appl. Phys. Rev.* **3**, 031106 (2016).
5. Singh, K. & Blanford, C. F. Electrochemical Quartz Crystal Microbalance with Dissipation Monitoring: A Technique to Optimize Enzyme Use in Bioelectrocatalysis. *ChemCatChem* **6**, 921–929 (2014).
6. Macchia, E. *et al.* About the amplification factors in organic bioelectronic sensors. *Mater. Horiz.* **7**, 999–1013 (2020).
7. Thompson, M. *et al.* Label-free detection of nucleic acid and protein microarrays by scanning Kelvin nanoprobe. *Biosens. Bioelectron.* **20**, 1471–1481 (2005).
8. Macchia, E. *et al.* Large-Area Interfaces for Single-Molecule Label-free Bioelectronic Detection. *Chem. Rev.* **122**, 4636–4699 (2022).
9. Di Franco, C. *et al.* Extended Work Function Shift of Large-Area Biofunctionalized Surfaces Triggered by a Few Single-Molecule Affinity Binding Events. *Adv. Mater. Interfaces* **10**, (2023).
10. Picca, R. A. *et al.* Ultimately Sensitive Organic Bioelectronic Transistor Sensors by Materials and Device Structure Design. *Adv. Funct. Mater.* **30**, (2020).
11. Estrela, P. *et al.* Label-Free Detection of Protein interactions with peptide aptamers by open circuit potential measurement. *Electrochim. Acta* **53**, 6489–6496 (2008).
12. Tsai, M.-Y. *et al.* Direct correlation between potentiometric and impedance biosensing of antibody-antigen interactions using an integrated system. *Appl. Phys. Lett.* **111**, (2017).
13. Goda, T. & Miyahara, Y. Molecularly Engineered Charge-Conversion of Proteins for Sensitive Biosensing. *Anal. Chem.* **82**, 8946–8953 (2010).
14. Mulla, M. Y. *et al.* Capacitance-modulated transistor detects odorant binding protein chiral interactions. *Nat. Commun.* **6**, 6010 (2015).
15. Costa, J. N. Y. *et al.* Single-Response Duplexing of Electrochemical Label-Free Biosensor from the Same Tag. *Adv. Healthc. Mater.* **13**, (2024).
16. Tao, W. *et al.* A sensitive DNA sensor based on an organic electrochemical transistor using a peptide nucleic acid-modified nanoporous gold gate electrode. *RSC Adv.* **7**, 52118–52124 (2017).
17. Yu, J. *et al.* Small Molecule-Driven Organic Electrochemical Transistors for Rapid, Ultrasensitive and Amplification-Free Detection of RNA Biomarkers. *Advanced Materials* **38**, (2026).
18. Liu, H. *et al.* Ultrafast, sensitive, and portable detection of COVID-19 IgG using flexible organic electrochemical transistors. *Sci. Adv.* **7**, (2021).

19. Bard, A. J. & Faulkner, L. R. *Electrochemical Methods : Fundamentals and Applications*. (Wiley, 2022).
20. Sheehan, P. E. & Whitman, L. J. Detection Limits for Nanoscale Biosensors. *Nano Lett.* **5**, 803–807 (2005).
21. Percival, S. J. & Bard, A. J. Ultra-Sensitive Potentiometric Measurements of Dilute Redox Molecule Solutions and Determination of Sensitivity Factors at Platinum Ultramicroelectrodes. *Anal. Chem.* **89**, 9843–9849 (2017).
22. Salvigni, L. *et al.* Reconfiguration of organic electrochemical transistors for high-accuracy potentiometric sensing. *Nat. Commun.* **15**, 6499 (2024).
23. Salvigni, L. *et al.* Selective detection of liposoluble vitamins using an organic electrochemical transistor. *Sens. Actuators B Chem.* **393**, 134313 (2023).
24. Mariani, F. *et al.* Microscopic Determination of Carrier Density and Mobility in Working Organic Electrochemical Transistors. *Small* **15**, (2019).
25. Lin, P., Luo, X., Hsing, I. & Yan, F. Organic Electrochemical Transistors Integrated in Flexible Microfluidic Systems and Used for Label-Free DNA Sensing. *Advanced Materials* **23**, 4035–4040 (2011).
26. Liang, Y., Wu, C., Figueroa-Miranda, G., Offenhäusser, A. & Mayer, D. Amplification of aptamer sensor signals by four orders of magnitude via interdigitated organic electrochemical transistors. *Biosens. Bioelectron.* **144**, 111668 (2019).
27. Nissa, J., Janson, P., Berggren, M. & Simon, D. T. The Role of Relative Capacitances in Impedance Sensing with Organic Electrochemical Transistors. *Adv. Electron. Mater.* **7**, (2021).
28. Yaghmazadeh, O. *et al.* Optimization of organic electrochemical transistors for sensor applications. *J. Polym. Sci. B Polym. Phys.* **49**, 34–39 (2011).
29. Wieland, M. *et al.* Conductance and spectroscopic mapping of EDOT polymer films upon electrochemical doping. *Flexible and Printed Electronics* **5**, 014016 (2020).
30. Schafer, E. A. *et al.* Sources and Mechanism of Degradation in p-Type Thiophene-Based Organic Electrochemical Transistors. *ACS Appl. Electron. Mater.* **4**, 1391–1404 (2022).
31. Keene, S. T. *et al.* Stable operating windows for polythiophene organic electrochemical transistors. *MRS Commun.* **14**, 158–166 (2023).
32. Nayak, P. D. *et al.* Understanding Oxygen-Induced Reactions and Their Impact on n-Type Polymeric Mixed Conductor-Based Devices. *ACS Cent. Sci.* **10**, 2229–2241 (2024).
33. Holze, R. Overoxidation of Intrinsically Conducting Polymers. *Polymers (Basel).* **14**, 1584 (2022).
34. Bernards, D. A. & Malliaras, G. G. Steady-State and Transient Behavior of Organic Electrochemical Transistors. *Adv. Funct. Mater.* **17**, 3538–3544 (2007).
35. Kahn, A. Fermi level, work function and vacuum level. *Mater. Horiz.* **3**, 7–10 (2016).
36. Strayer, R. W., Mackie, W. & Swanson, L. W. Work function measurements by the field emission retarding potential method. *Surf. Sci.* **34**, 225–248 (1973).